

Learning-based Multi-continuum Model for Multiscale Flow Problems

Fan Wang^a, Yating Wang^{a,*}, Wing Tat Leung^b and Zongben Xu^a

^a*School of Mathematics and Statistics, Xi'an Jiaotong University, Xi'an, China*

^b*Department of Mathematics, City University of Hong Kong, Hong Kong, Hong Kong Special Administrative Region*

ARTICLE INFO

Keywords:

Multiscale problems
Numerical homogenization
Multi-continuum model
Deep learning

ABSTRACT

Multiscale problems can usually be approximated through numerical homogenization by an equation with some effective parameters that can capture the macroscopic behavior of the original system on the coarse grid to speed up the simulation. However, this approach usually assumes scale separation and that the heterogeneity of the solution can be approximated by the solution average in each coarse block. For complex multiscale problems, the computed single effective properties/continuum might be inadequate. In this paper, we propose a novel learning-based multi-continuum model to enrich the homogenized equation and improve the accuracy of the single continuum model for multiscale problems with some given data. Without loss of generalization, we consider a two-continuum case. The first flow equation keeps the information of the original homogenized equation with an additional interaction term. The second continuum is newly introduced, and the effective permeability in the second flow equation is determined by a neural network. The interaction term between the two continua aligns with that used in the Dual-porosity model but with a learnable coefficient determined by another neural network. The new model with neural network terms is then optimized using trusted data. We discuss both direct back-propagation and the adjoint method for the PDE-constraint optimization problem. Our proposed learning-based multi-continuum model can resolve multiple interacted media within each coarse grid block and describe the mass transfer among them, and it has been demonstrated to significantly improve the simulation results through numerical experiments involving both linear and nonlinear flow equations.

1. Introduction

Multiscale flow problems occur naturally across various physical and engineering applications. The subsurface formation of the flow problem usually involves discrete fractures and faults. Modeling and simulating processes within such fractured media presents difficulties due to the complexity of material properties, such as thermal diffusivity or hydraulic conductivity. The substantial differences between the fractures and the background pose challenges in numerical simulation since the high-contrast feature of the heterogeneous media introduces stiffness in the system and leads to a heavy computational burden for full fine-scale computation.

Multiscale model reduction methods, including local [2, 1, 6, 16] and global approaches [22, 14, 10, 12], have been proposed to reduce computational costs in the numerical simulation of multiscale problems. The main idea is to construct reduced-order models to approximate the full fine-scale model to achieve efficient computation. Many local model reduction approaches, such as numerical homogenization [7, 31, 5, 24, 18], multiscale finite element methods [17, 15], variational multiscale methods [23], heterogeneous multiscale methods [4], localized orthogonal decomposition [29, 20, 21], etc, have been successfully applied in many applications.

Among these, numerical homogenization methods/flow-based upscaling methods are classic ways of solving multiscale problems. They calculate effective properties, such as permeability, in each coarse block that is comprised of an agglomeration of fine grid blocks, to incorporate fine-scale information into coarse-scale properties. Through the homogenization process, a complex multiscale system is approximated by a simple homogenized equation in which the heterogeneous microstructure is replaced by an equivalent homogeneous macrostructure. This homogenized equation can be numerically solved on a coarse mesh in a fast manner.

*Corresponding author

✉ wangfan525@stu.xjtu.edu.cn (F. Wang); yatingwang@xjtu.edu.cn (Y. Wang); wtleung27@cityu.edu.hk (W.T. Leung); zbxu@mail.xjtu.edu.cn (Z. Xu)

ORCID(s):

However, the standard numerical homogenization is insufficient for multiple interacted media. A multiple continua approach is needed. The multi-continuum model [9, 3, 8, 37] is proposed by considering multiple interconnected parallel systems that are distributed all over the domain in the flow field. The dual-porosity model [9] is the first multi-continuum model in which the flow equations for the background (called the matrix) and the fracture are written separately with some interaction. In these approaches, several effective properties need to be computed locally in each coarse block, and some transfer terms are introduced to model the interaction. The transfer coefficients in the multi-continuum model are usually obtained based on simplified physical assumptions.

For complicated physical processes, the above-mentioned reduced order models might be inadequate due to ignoring microscopic information or physical simplifying assumptions. Thus resulting in non-negligible errors between the simulation results obtained from the reduced order models and the real observation data. In this paper, we will consider improving a given inaccurate reduced order model with trusted data by a deep learning approach.

Recently, leveraging the deep learning approach to assist scientific computing has been an emerging trend. Many works have been done to apply neural networks to approximate the solutions of partial differential equations (PDEs), such as PINN [32], deep Ritz method [39], deep Galerkin method [35], etc. For parameterized PDEs, operator learning approaches such as DeepOnet [28] and Fourier Neural Operator [27] have been developed to learn the mapping from the parameter space to the solutions space. Other deep learning approaches for PDE-related tasks include developing surrogate models motivated by classical numerical solvers. For example, in [19, 40], the authors construct multiscale neural networks based on hierarchical multigrid solvers and encoder-decoder neural networks for solutions of heterogeneous elliptic PDEs. There are also other deep learning approaches to handle multiscale problems. For instance, some data-driven methods are proposed to obtain the coarse grid effective properties based on the nonlocal multi-continuum upscaling method [36], and the coefficients in global model reduction techniques such as the proper orthogonal decomposition (POD) projection [13]. Furthermore, a neural homogenization-based PINN (NH-PINN) [26] was investigated to improve the PINN accuracy for solving multiscale problems with the help of homogenization. The idea is to use PINN to solve the cell problems and the homogenized coefficients can be evaluated to form the homogenized equation. Then, PINN is utilized again to solve the global homogenized equation. However, in the above methods, the physical model is assumed to be accurate, and deep learning methods are used to learn the solution of the underlying physical model.

Another area of research involves representing unknown or omitted physical processes by deep learning methods, in order to correct the original PDE to make them more accurate and easier to solve. These unrepresented or unknown physics are typically challenging to express due to limited cognition or computational cost. The deep learning PDE augmentation method (DPM) [34] leverages known physics (expressed in a PDE) to learn closures for unknown or unrepresented physics. For the large-eddy simulation of turbulence, DPM indicates that the neural network can acquire a more effective sub-filter-scale closure than conventional LES models, which enhances numerical accuracy. The approaches in [30, 38] employ neural networks to approximate the collision operator of the Boltzmann equation. Because of the extremely high dimensionality and nonlinearity, this collision operator poses a notorious challenge for theoretical analysis and numerical simulation. Compared with the classical simplified model, the neural network-based model of a collision operator not only agrees with the direct simulation but also maintains the essential structural properties of a many-particle system. The study in [33] presents a theoretical analysis of the convergence of optimizing neural network terms of linear elliptic PDEs by the adjoint method.

In this paper, we proposed a novel learning-based multi-continuum model, to enrich the homogenized equation and address the inaccuracy of PDE solutions caused by numerical homogenization for multiscale problems. Without loss of generalization, we consider a two-continuum case. We remodel the homogenized single continuum equation as a multi-continuum model, where the homogenized equation serves as the flow equation for the first continuum with an additional interaction term. For the newly introduced second continuum, the effective permeability of its flow equation is determined by a neural network. The interaction term of these two continua aligns with that used in the Dual-porosity model but with a learnable coefficient determined by another neural network. By optimizing networks through the trusted data, our learning-based multi-continuum model improves the accuracy of solutions for the original homogenized equation. Additionally, we discuss both direct back-propagation and the adjoint method for the PDE-constraint optimization problem. The main contributions of this paper are summarized as follows.

- We propose a new learning-based multi-continuum model to correct the homogenized flow equation with given data and improve the accuracy of the solution for multiscale problems.

- We consider both direct back-propagation and the adjoint method to compute the gradients of the loss function with respect to the network parameters to optimize our proposed learning-based multi-continuum model.
- We conducted numerical experiments including linear and nonlinear flow equations. Our proposed model can substantially improve the accuracy of the solution of the reduced order model obtained from standard numerical homogenization.

The rest of the paper is organized as follows. In Section 2, we review the basics of the multiscale flow problem, the reduced-order model with numerical homogenization, and the multi-continuum model. Next, we will present our proposed learning-based multi-continuum model in Section 3. We conduct several numerical experiments in Section 4. Conclusions are given in Section 5.

2. Background

2.1. Multiscale flow problem

Consider the parabolic equation

$$\begin{aligned} \frac{\partial u(\mathbf{x}, t)}{\partial t} - \operatorname{div}(\kappa(\mathbf{x}, u(\mathbf{x}, t))\nabla u(\mathbf{x}, t)) &= f(\mathbf{x}, t), & \text{in } \Omega \times [0, T], \\ u(\mathbf{x}, t) &= 0, & \text{in } \Omega \times \{0\}, \\ u(\mathbf{x}, t) &= 0, & \text{on } \partial\Omega \times [0, T], \end{aligned} \quad (2.1)$$

where $u(\mathbf{x}, t) \in \mathbb{R}$ is the solution, $\mathbf{x} \in \Omega \subset \mathbb{R}^d$, $T > 0$ is the final time. The nonlinear diffusion coefficient $\kappa(\mathbf{x}, u(\mathbf{x}, t))$ represents the conductivity/permeability of the underlying field, and we assume $\kappa(\mathbf{x}, u(\mathbf{x}, t)) = \kappa_0(\mathbf{x})\kappa_u(u(\mathbf{x}, t))$. In particular, assume $\kappa_u(u(\mathbf{x}, t)) > 0$ and is bounded and Lipschitz continuous, and $\kappa_0 \in L^\infty(\Omega)$ is the value of the conductivity/permeability of a fractured/channelized media. Since the material properties within fractures can be very different from the background properties and the complex fracture configuration, there are multiple scales and high contrast of κ_0 . The multiscale and nonlinear feature poses the challenges in the numerical simulation.

2.2. Reduced order model with numerical homogenization – single continuum

Numerical homogenization is a classic model reduction approach to finding numerical solutions of heterogeneous multiscale problems. It approximates the original multiscale problem with a simpler homogenized one. The solution of this homogenized equation can capture the macroscopic behavior of the original multiscale problem. The parameters of the homogenized equation (such as permeability) are normally homogeneous or smooth, such that the homogenized equation can be solved numerically in a coarse mesh.

To illustrate the idea, we here give the numerical homogenization of the parabolic equation with the coefficients that has two scales \mathbf{x} and $\mathbf{y} = \mathbf{x}/\epsilon$,

$$\frac{\partial u_\epsilon}{\partial t} - \frac{\partial}{\partial x_i}(\kappa_{ij}(\mathbf{x}, \mathbf{x}/\epsilon)\frac{\partial}{\partial x_j})u_\epsilon = f, \quad (\mathbf{x}, t) \in \Omega \times [0, T], \quad (2.2)$$

with $u_\epsilon(\mathbf{x}, t) = 0$ on $\partial\Omega$ or $t = 0$. Here we use the Einstein notation. We seek for $u_\epsilon(\mathbf{x}, t)$ in the asymptotic expansion

$$u_\epsilon(\mathbf{x}, t) = u_0(\mathbf{x}, \mathbf{x}/\epsilon, t) + \epsilon u_1(\mathbf{x}, \mathbf{x}/\epsilon, t) + \epsilon^2 u_2(\mathbf{x}, \mathbf{x}/\epsilon, t) + \mathcal{O}(\epsilon^3), \quad (2.3)$$

where $u_j(\mathbf{x}, \mathbf{x}/\epsilon, t)$, for $j = 0, 1, 2, \dots$, are periodic in $\mathbf{y} = \mathbf{x}/\epsilon$. Denoted by A^ϵ the second-order elliptic operator

$$A^\epsilon = -\frac{\partial}{\partial x_i}(\kappa_{ij}(\mathbf{x}, \mathbf{x}/\epsilon)\frac{\partial}{\partial x_j}). \quad (2.4)$$

With this notation, it can be checked that

$$A^\epsilon = \epsilon^{-2}A_1 + \epsilon^{-1}A_2 + \epsilon^0A_3, \quad (2.5)$$

where

$$\begin{aligned}
 A_1 &= -\frac{\partial}{\partial y_i}(\kappa_{ij}(\mathbf{x}, \mathbf{y}) \frac{\partial}{\partial y_j}), \\
 A_2 &= -\frac{\partial}{\partial y_i}(\kappa_{ij}(\mathbf{x}, \mathbf{y}) \frac{\partial}{\partial x_j}) - \frac{\partial}{\partial x_i}(\kappa_{ij}(\mathbf{x}, \mathbf{y}) \frac{\partial}{\partial y_j}), \\
 A_3 &= -\frac{\partial}{\partial x_i}(\kappa_{ij}(\mathbf{x}, \mathbf{y}) \frac{\partial}{\partial x_j}).
 \end{aligned} \tag{2.6}$$

We hence have $A^\epsilon u_\epsilon = f$. By equating the terms of different powers of ϵ , we have

$$\begin{aligned}
 A_1 u_0 &= 0, \\
 A_1 u_1 + A_2 u_0 &= 0, \\
 A_1 u_2 + A_2 u_1 + A_3 u_0 - f &= -\frac{\partial u_0}{\partial t}.
 \end{aligned} \tag{2.7}$$

Substitute A_1 into the first equation of (2.7), we can obtain

$$-\frac{\partial}{\partial y_i}(\kappa_{ij}(\mathbf{x}, \mathbf{y}) \frac{\partial}{\partial y_j}) u_0(\mathbf{x}, \mathbf{y}, t) = 0 \tag{2.8}$$

where u_0 is periodic in \mathbf{y} . The theory of second-order elliptic PDEs implies that $u_0(\mathbf{x}, \mathbf{y}, t)$ is independent of \mathbf{y} , i.e., $u_0(\mathbf{x}, \mathbf{y}, t) = u_0(\mathbf{x}, t)$. This leads to

$$-\frac{\partial}{\partial y_i}(\kappa_{ij}(\mathbf{x}, \mathbf{y}) \frac{\partial}{\partial y_j}) u_1 = \left(\frac{\partial}{\partial y_i} \kappa_{ij}(\mathbf{x}, \mathbf{y}) \right) \frac{\partial u_0(\mathbf{x}, t)}{\partial x_j}. \tag{2.9}$$

Define $\mathcal{N}_j = \mathcal{N}_j(\mathbf{x}, \mathbf{y})$ as the solution to the following *cell problem*:

$$-\frac{\partial}{\partial y_i}(\kappa_{ij}(\mathbf{x}, \mathbf{y}) \frac{\partial}{\partial y_j}) \mathcal{N}_j = \frac{\partial}{\partial y_i} \kappa_{ij}(\mathbf{x}, \mathbf{y}), \tag{2.10}$$

where \mathcal{N}_j is periodic in \mathbf{y} . The general solution for u_1 is then given by

$$u_1(\mathbf{x}, \mathbf{y}, t) = \mathcal{N}_j(\mathbf{x}, \mathbf{y}) \frac{\partial u_0(\mathbf{x}, t)}{\partial x_j}. \tag{2.11}$$

Finally, we note that the equation for u_2 is given by

$$\frac{\partial}{\partial y_i}(\kappa_{ij}(\mathbf{x}, \mathbf{y}) \frac{\partial}{\partial y_j}) u_2 = A_2 u_1 + A_3 u_0 - f + \frac{\partial u_0}{\partial t}. \tag{2.12}$$

The solvability condition implies that the right-hand side of (2.12) must have mean zero in \mathbf{y} over one periodic cell $Y = [0, 1] \times [0, 1]$, i.e.,

$$\int_Y (A_2 u_1 + A_3 u_0 - f + \frac{\partial u_0}{\partial t}) d\mathbf{y} = 0. \tag{2.13}$$

Next, a different trick is used. In particular, the equation at ϵ^0 is averaged over the period. We note that

$$\left\langle \frac{\partial}{\partial y_i} F(\mathbf{x}, \mathbf{y}, t) \right\rangle = \int_Y \frac{\partial}{\partial y_i} F(\mathbf{x}, \mathbf{y}, t) d\mathbf{y} = 0, \tag{2.14}$$

for any $F(\mathbf{x}, \mathbf{y}, t)$ which is periodic with respect to \mathbf{y} . This can be easily verified using the divergence theorem. Then, the averages over the terms which start with $\frac{\partial}{\partial y_i}$ will disappear and we get

$$\frac{\partial u_0}{\partial t} - \frac{\partial}{\partial x_i} \left(\left\langle \kappa_{ij}(\mathbf{x}, \mathbf{y}) \right\rangle \frac{\partial}{\partial x_j} u_0 \right) - \frac{\partial}{\partial x_i} \left\langle \kappa_{ij}(\mathbf{x}, \mathbf{y}) \frac{\partial}{\partial y_j} u_1 \right\rangle = f. \tag{2.15}$$

Substituting the expression for u_1 into this equation, we obtain

$$\frac{\partial u_0}{\partial t} - \frac{\partial}{\partial x_i} (\kappa_{ij}^* \frac{\partial}{\partial x_j}) u_0 = f, \quad (2.16)$$

where

$$\kappa_{ij}^* = \frac{1}{|Y|} \int_Y (\kappa_{ij} + \kappa_{ik} \frac{\partial \mathcal{N}_j}{\partial y_k}) d\mathbf{y}. \quad (2.17)$$

The homogenized equation of the multiscale flow problem (2.1) is then given by

$$\frac{\partial u(\mathbf{x}, t)}{\partial t} - \text{div}(\kappa^* \nabla u(\mathbf{x}, t)) = f(\mathbf{x}, t) \quad \text{in } \Omega \times [0, T], \quad (2.18)$$

where κ^* is the homogenized value of the permeability. The homogenized solution is a kind of local average of the solution of the original multiscale equation. This homogenized solution approximates the original solution and can capture the macroscopic behavior of the original multiscale problem. We build on the homogenized equation as a good initialization and further correct it to obtain a more accurate model for characterizing the complex dynamics of multiscale problems.

2.3. Multi-continuum model.

The numerical homogenization technique is widely used for single continuum upscaling. However, in a more general setup, a multi-continuum approach is needed. The multi-continuum model divides a material or medium into multiple regions with different physical properties between each region. These regions can have different structures, compositions, porosities, temperatures, and so on. The model describes the behavior of the whole system by defining the specific physical properties of each region (for example, fluid flow, heat transfer, mass transport, etc.) and the interactions between them. By incorporating various physical processes and considering the mutual coupling between regions, multi-continuum models can more accurately capture the macroscopic behavior of a complicated material or medium.

A coupled system of dual-continuum equations for the multiscale flow equation has the form

$$\begin{aligned} \frac{\partial u_1(\mathbf{x}, t)}{\partial t} - \text{div}(\kappa_1(\mathbf{x}, u_1(\mathbf{x}, t)) \nabla u_1(\mathbf{x}, t)) + \sigma_{12}(\mathbf{x}, u_1(\mathbf{x}, t), u_2(\mathbf{x}, t))(u_1(\mathbf{x}, t) - u_2(\mathbf{x}, t)) &= f_1(\mathbf{x}, t), \\ \frac{\partial u_2(\mathbf{x}, t)}{\partial t} - \text{div}(\kappa_2(\mathbf{x}, u_2(\mathbf{x}, t)) \nabla u_2(\mathbf{x}, t)) + \sigma_{21}(\mathbf{x}, u_2(\mathbf{x}, t), u_1(\mathbf{x}, t))(u_2(\mathbf{x}, t) - u_1(\mathbf{x}, t)) &= f_2(\mathbf{x}, t), \end{aligned} \quad (2.19)$$

where $(\mathbf{x}, t) \in \Omega \times [0, T]$, u_i denotes the solution for the i -th continuum, κ_i denotes the value of permeability, f_i represents the source function for the i th continuum, $i = 1, 2$. Terms $\sigma_{12}(\mathbf{x}, u_1, u_2)(u_1 - u_2)$ and $\sigma_{21}(\mathbf{x}, u_2, u_1)(u_2 - u_1)$ describe mass transfer of the liquid which flows from one continuum into another continuum per unit of media volume as well as per unit of time. However, it is usually difficult to capture the transient fluid transfer between different continua, and the transfer coefficients σ_{12} and σ_{21} are typically determined empirically.

3. Method

In this section, we present our proposed approach to model correction based on the deep learning method. We propose to rectify the inaccuracy of numerical homogenization of the highly heterogeneous multiscale flow equation, especially the ones that possess multi-continuum properties in the underlying media, using a learning-based multi-continuum model. Our model involves learning the permeability in the new continuum and transfer coefficient from the trusted data. **Figure 1** illustrates our methodology. The permeability and transfer coefficient are parameterized as neural networks. The network parameters can be optimized by aligning the numerical solutions of the corrected model with trusted data. To optimize the networks, we have selected two methods to calculate the gradients of the network: direct back-propagation (BP) with the automatic differentiation of Tensorflow/Pytorch and the adjoint method. The adjoint method computes the loss function's derivatives relative to the network parameters by solving the adjoint equation, thus eliminating the need for abundant storage in the forward solver. However, computing the solutions to the adjoint equations also introduces additional computational costs. In the following subsections, we introduce our learning-based multi-continuum model, as well as the forward PDE solvers and optimization methods for linear and non-linear problems, respectively.

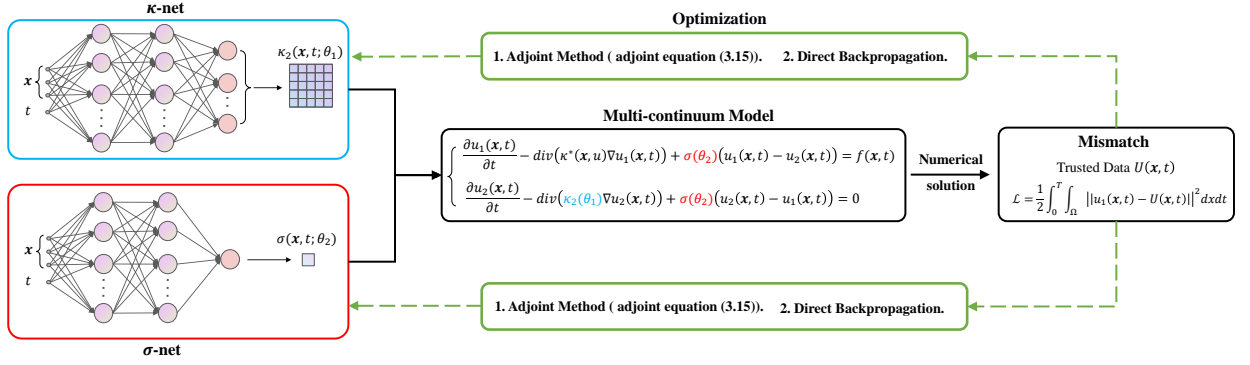


Figure 1: The schematic illustration of our proposed learning-based multi-continuum model. The black color indicates the forward process, and the green color indicates the back-propagation to optimize network parameters.

3.1. Learning-based multi-continuum model

Numerical homogenization captures the macroscopic behavior of the original complicated multiscale flow equation and generates solutions with low precision. To increase the accuracy of solutions, we propose to use a multi-continuum model to enrich the homogenized equation (2.18), which is formulated as

$$\begin{aligned} \frac{\partial u_1(\mathbf{x}, t)}{\partial t} - \operatorname{div}(\kappa_1^*(\mathbf{x}, u_1) \nabla u_1(\mathbf{x}, t)) + \sigma(\mathbf{x}, u_1, u_2)(u_1(\mathbf{x}, t) - u_2(\mathbf{x}, t)) &= f(\mathbf{x}, t), & \text{in } \Omega \times [0, T], \\ \frac{\partial u_2(\mathbf{x}, t)}{\partial t} - \operatorname{div}(\kappa_2(\mathbf{x}, u_2) \nabla u_2(\mathbf{x}, t)) + \sigma(\mathbf{x}, u_1, u_2)(u_2(\mathbf{x}, t) - u_1(\mathbf{x}, t)) &= 0, & \text{in } \Omega \times [0, T], \end{aligned} \quad (3.1)$$

where u_1 corresponds to the solution of the homogenized flow equation, κ_1^* denotes the homogenized permeability, u_2 is the solution of the flow equation in the introduced second continuum, $\kappa_2(\mathbf{x}, u_2)$ denotes the permeability of the second continuum, and $\sigma(\mathbf{x}, u_1, u_2)$ is the transfer coefficient. The source term for the second continuum's flow equation is set to 0. The initial and boundary conditions of this multi-continuum model are given by

$$u_1(\mathbf{x}, t = 0) = u_2(\mathbf{x}, t = 0) = 0, \quad \text{in } \Omega, \quad u_1(\mathbf{x}, t) = u_2(\mathbf{x}, t) = 0, \quad \text{on } \partial\Omega \times [0, T].$$

In model (3.1), both the permeability field κ_2 and the transfer coefficient σ are unknown and need to be determined. For the newly introduced continuum, we do not know its properties. Thus we propose to leverage the deep learning method to determine the values of the permeability field κ_2 and the transfer coefficient σ . The schematic illustration of our method is shown in **Figure 1**. Specifically, the learning-based multi-continuum model is defined as

$$\begin{aligned} \frac{\partial u_1(\mathbf{x}, t)}{\partial t} - \operatorname{div}(\kappa_1^*(\mathbf{x}, u_1) \nabla u_1(\mathbf{x}, t)) + \sigma(\mathbf{x}, t; \theta_2)(u_1(\mathbf{x}, t) - u_2(\mathbf{x}, t)) &= f(\mathbf{x}, t), & \text{in } \Omega \times [0, T], \\ \frac{\partial u_2(\mathbf{x}, t)}{\partial t} - \operatorname{div}(\kappa_2(\mathbf{x}, t; \theta_1) \nabla u_2(\mathbf{x}, t)) + \sigma(\mathbf{x}, t; \theta_2)(u_2(\mathbf{x}, t) - u_1(\mathbf{x}, t)) &= 0, & \text{in } \Omega \times [0, T], \end{aligned} \quad (3.2)$$

where $\kappa_2(\mathbf{x}, t; \theta_1)$ and $\sigma(\mathbf{x}, t; \theta_2)$ are parameterized as neural networks, named κ -net and σ -net respectively, θ_1 and θ_2 are network parameters. The κ -net $\kappa_2(\mathbf{x}, t; \theta_1) : \mathbb{R}^{d+1} \rightarrow \mathbb{R}^{d \times d}$ learns elements of the permeability matrix of the second continuum at each coordinate \mathbf{x} and time t . It corrects the solution u_1 by controlling the dynamics of u_2 in the second newly introduced continuum. The σ -net $\sigma(\mathbf{x}, t; \theta_2) : \mathbb{R}^{d+1} \rightarrow \mathbb{R}$ learns a transfer coefficient to determine the impact of u_2 on the solution u_1 .

In this way, we obtain a learning-based multi-continuum model that corrects the original homogenized equation. Its numerical solution can be obtained by classical methods (such as finite difference method (FDM) and finite element method (FEM)) and deep learning methods (PINN, DeepRitz, etc.). The network parameters θ_1 and θ_2 are optimized by minimizing the mismatch between the numerical solution and the trusted data, i.e. minimizing the loss function

$$\mathcal{L} = \frac{1}{2} \int_0^T \int_{\Omega} \|u_1(\mathbf{x}, t) - U(\mathbf{x}, t)\|^2 d\mathbf{x} dt, \quad (3.3)$$

where $U(\mathbf{x}, t)$ denotes the trusted data of the multiscale flow equation (2.1) assumed to be available at certain coordinates and times. By minimizing the loss function (3.3), the permeability field κ_2 and transfer coefficient σ can be determined and we obtain a new multi-continuum model that more accurately models the dynamics of the flow in the heterogeneous media.

3.2. Forward solver

The calculation of the loss function (3.3) requires the numerical solutions of equation (3.2). In this section, we present our numerical solver for linear and nonlinear equations. FEM is the basic solver used in our method. In addition, we propose to use the deep learning method, PINN, to solve the nonlinear equation to simplify the arduous iterations. Details are as follows.

3.2.1. Linear flow equation

For the linear flow equation, we assume the values of permeability only dependent on the coordinate \mathbf{x} , i.e.,

$$\frac{\partial u(\mathbf{x}, t)}{\partial t} - \operatorname{div}(\kappa(\mathbf{x})\nabla u(\mathbf{x}, t)) = f(\mathbf{x}, t), \quad \text{in } \Omega \times [0, T]. \quad (3.4)$$

The corresponding learning-based two-continuum correction model is reformulated as

$$\begin{aligned} \frac{\partial u_1(\mathbf{x}, t)}{\partial t} - \operatorname{div}(\kappa_1^*(\mathbf{x})\nabla u_1(\mathbf{x}, t)) + \sigma(\mathbf{x}; \theta_2)(u_1(\mathbf{x}, t) - u_2(\mathbf{x}, t)) &= f(\mathbf{x}, t), \quad \text{in } \Omega \times [0, T], \\ \frac{\partial u_2(\mathbf{x}, t)}{\partial t} - \operatorname{div}(\kappa_2(\mathbf{x}; \theta_1)\nabla u_2(\mathbf{x}, t)) + \sigma(\mathbf{x}; \theta_2)(u_2(\mathbf{x}, t) - u_1(\mathbf{x}, t)) &= 0, \quad \text{in } \Omega \times [0, T], \end{aligned} \quad (3.5)$$

where the permeability κ_2 and transfer coefficient σ are only dependent on the coordinate \mathbf{x} . We solve equation (3.5) by FEM. The weak form of equation (3.5) is to seek $u_1(t, \cdot), u_2(t, \cdot) \in V = H_0^1(\Omega)$ such that for $\forall v_1, v_2 \in V$,

$$\begin{aligned} \left(\frac{\partial u_1}{\partial t}, v_1\right) + a_1(u_1, v_1) + (\sigma(u_1 - u_2), v_1) &= (f, v_1), \quad t \in (0, T], \\ \left(\frac{\partial u_2}{\partial t}, v_2\right) + a_2(u_2, v_2) + (\sigma(u_2 - u_1), v_2) &= 0, \quad t \in (0, T], \end{aligned} \quad (3.6)$$

where $a_1(u_1, v_1) = \int_{\Omega} \kappa_1^* \nabla u_1 \cdot \nabla v_1 d\mathbf{x}$ and $a_2(u_2, v_2) = \int_{\Omega} \kappa_2 \nabla u_2 \cdot \nabla v_2 d\mathbf{x}$. Now consider a spatial partition Γ_h of the computational domain Ω , h denotes the mesh size. We choose the linear basis function ψ_i and form the space $V_h = \operatorname{span}\{\psi_i, 1 \leq i \leq L\}$. Then the discretization of (3.6) reads as

$$\begin{aligned} M \frac{\partial u_1}{\partial t} + A_1(\kappa_1^*)u_1 + \sigma(\mathbf{x}, \theta_2)M(u_1 - u_2) &= F, \\ M \frac{\partial u_2}{\partial t} + A_2(\kappa_2(\mathbf{x}, \theta_1))u_2 + \sigma(\mathbf{x}, \theta_2)M(u_2 - u_1) &= 0, \end{aligned} \quad (3.7)$$

where M is the mass matrix whose elements are $\int_{\Omega} \psi_i \psi_j d\mathbf{x}$, A_1 and A_2 are the stiffness matrices with elements $\int_{\Omega} \kappa_1^* \nabla \psi_i \cdot \nabla \psi_j d\mathbf{x}$ and $\int_{\Omega} \kappa_2 \nabla \psi_i \cdot \nabla \psi_j d\mathbf{x}$ respectively, and the elements of F are $\int_{\Omega} f \psi_j d\mathbf{x}$. We use implicit backward Euler scheme in time

$$\begin{aligned} M \frac{u_1^{k+1} - u_1^k}{\tau} + A_1(\kappa_1^*)u_1^{k+1} + \sigma(\mathbf{x}, \theta_2)M(u_1^{k+1} - u_2^{k+1}) &= F^{k+1}, \\ M \frac{u_2^{k+1} - u_2^k}{\tau} + A_2(\kappa_2(\mathbf{x}, \theta_1))u_2^{k+1} + \sigma(\mathbf{x}, \theta_2)M(u_2^{k+1} - u_1^{k+1}) &= 0, \end{aligned} \quad (3.8)$$

where $u^k = u(t_k)$ and $t_k = k\tau, k = 0, 1, \dots, N_t - 1, N_t = T/\tau$ is the number of time steps. For each time step k , the numerical solution of u_1 can be obtained by solving the above linear system.

3.2.2. Nonlinear equation

For the nonlinear multiscale flow equation (2.1), we introduce two different methods, the classical FEM with iteration approach and the deep learning method PINN, to solve the learning-based multi-continuum model (3.2).

Finite element method. The discretization of equation (3.2) in FEM with implicit backward Euler scheme in time is formulated as

$$\begin{aligned} M \frac{u_1^{k+1} - u_1^k}{\tau} + A_1^{k+1}(\kappa_1^*)u_1^{k+1} + \sigma^{k+1}(\mathbf{x}, t, \theta_2)M(u_1^{k+1} - u_2^{k+1}) &= F^{k+1}, \\ M \frac{u_2^{k+1} - u_2^k}{\tau} + A_2^{k+1}(\kappa_2(\mathbf{x}, t, \theta_1))u_2^{k+1} + \sigma^{k+1}(\mathbf{x}, t, \theta_2)M(u_2^{k+1} - u_1^{k+1}) &= 0, \end{aligned} \quad (3.9)$$

where A_1^{k+1} is dependent on u_1^{k+1} and are different for each $k = 0, 2, \dots, N_t - 1$. The equation of u_2 is linear and A_2^{k+1} we learned only determined by coordinate \mathbf{x} and time t . In this paper, we use the Newton-Raphson method to solve the above nonlinear equation. This procedure employs a first order approximation of (3.9) in the neighbourhood of an approximate solution $u_1^{k+1;n}$ resulting in a linear system. For an approximate solution $u_1^{k+1;n}$, $n = 1, 2, \dots, N$, we calculate the solution $u_2^{k+1;n}$ by

$$M \frac{u_2^{k+1;n} - u_2^{k;n}}{\tau} + A_2^{k+1}(\kappa_2(\mathbf{x}, t, \theta_1))u_2^{k+1;n} + \sigma^{k+1}(\mathbf{x}, t, \theta_2)M(u_2^{k+1;n} - u_1^{k+1;n}) = 0, \quad (3.10)$$

Then the approximate solution $u_1^{k+1;n}$ is updated according to

$$u_1^{k+1;n+1} = u_1^{k+1;n} + \delta u_1, \quad (3.11)$$

where δu_1 can be computed by

$$\left(\frac{1}{\tau} M + \partial_{u_1^{k+1;n}} A_1^{k+1;n}(\kappa_1^*)u_1^{k+1;n} + A_1^{k+1;n}(\kappa_1^*) + \sigma^{k+1}(\mathbf{x}, t, \theta_2)M \right) \delta u_1 = -R_1^{k+1;n}, \quad (3.12)$$

where $A_1^{k+1;n}$ is the stiff matrix at $u_1^{k+1;n}$, and $R_1^{k+1;n}$ is the residuals of (3.9) at $u_1^{k+1;n}, u_2^{k+1;n}$. These so-called iterations are repeated until the residual of equation (3.9) is satisfied with sufficient precision.

Although the nonlinear multi-continuum model (3.2) can be solved by utilizing the FEM and Newton-Raphson method, the latter involves numerous iterations which in turn result in high computational cost. Additionally, the backpropagation and adjoint method used to optimize the network parameters, as introduced in Section 3.3, also incur significant computation costs, due to multiple iterations in the Newton-Raphson method. Therefore, we have opted to employ the deep learning method, PINN, to solve the nonlinear equation (3.2).

Physics-informed neural network (PINN). PINN is adopted as our forward solver for the nonlinear multiscale flow equation. It directly maps from the coordinate \mathbf{x} and time t to the desired solution. We denote the PINN solver as $\text{PINN}(\theta_3)$ where θ_3 is the network parameter. By this way, the parameters θ_1, θ_2 of κ -net, σ -net, and parameters θ_3 of PINN need to be optimized simultaneously. The loss function is reformulated as

$$\begin{aligned} \mathcal{L}(\theta_1, \theta_2, \theta_3) &= \frac{1}{2} \int_0^T \int_{\Omega} \|u_1(\mathbf{x}, t) - U(\mathbf{x}, t)\|^2 d\mathbf{x} dt \\ &+ \int_0^T \int_{\Omega} \left\| \frac{\partial u_1}{\partial t} - \text{div}(\kappa_1^* \nabla u_1) + \sigma(\mathbf{x}, t; \theta_2)(u_1 - u_2) - f \right\|^2 d\mathbf{x} dt \\ &+ \int_0^T \int_{\Omega} \left\| \frac{\partial u_2}{\partial t} - \text{div}(\kappa_2(\mathbf{x}, t; \theta_1) \nabla u_2) + \sigma(\mathbf{x}, t; \theta_2)(u_2 - u_1) \right\|^2 d\mathbf{x} dt, \end{aligned} \quad (3.13)$$

where $u_1, u_2 = \text{PINN}(\mathbf{x}, t; \theta_3)$ are solutions obtained by the PINN solver. The PINN solver avoids the cumbersome iterations of the Newton-Raphson method.

3.3. Optimization method

The network parameters can be optimized by minimizing the loss function (3.3) through the gradient descent method,

$$\theta_{k+1} = \theta_k - \alpha_k \nabla_{\theta} \mathcal{L}(\theta), \quad k = 0, 1, \dots, K, \quad (3.14)$$

where θ denotes parameters θ_1, θ_2 and θ_3 (for nonlinear problem), α_k is the learning rate and K is the total number of optimization steps. This requires calculating the gradient $\nabla_{\theta} \mathcal{L}(\theta)$ which depends upon the solution of PDE (3.2). The most straightforward method for computing the gradient is via the automatic differentiation of Tensorflow/Pytorch. Nevertheless, this technique incurs high computational and storage costs since the intermediate quantities of the iterations in our forward PDE solver, FEM, must be preserved to calculate the gradient. In the following, we derive the adjoint method for optimizing the linear multi-continuum model (3.5). In the nonlinear problem with the forward solver PINN, the network parameters are optimized through **direct BP**. **Direct BP** denotes that the gradients of the loss function with respect to the network parameters are calculated by the automatic differentiation, as opposed to the adjoint method.

Optimization for linear equation. The adjoint method [11] provides a computationally efficient way to calculate gradients for PDE-constrained optimization problems. It requires solving the adjoint PDE per parameter update. The dimension of the adjoint PDE matches the dimension PDE (3.2). The adjoint PDE of equation (3.2) is given by

$$\begin{aligned} \frac{\partial \lambda_1}{\partial t} + \operatorname{div}(\kappa_1^*(\mathbf{x}) \nabla \lambda_1) - \sigma(\mathbf{x}; \theta_2)(\lambda_1 - \lambda_2) &= u_1(\mathbf{x}, t) - U(\mathbf{x}, t), \\ \frac{\partial \lambda_2}{\partial t} + \operatorname{div}(\kappa_2(\mathbf{x}; \theta_1) \nabla \lambda_2) - \sigma(\mathbf{x}; \theta_2)(\lambda_2 - \lambda_1) &= 0, \end{aligned} \quad (3.15)$$

where λ_1 and λ_2 are the adjoint variable which are functions of coordinate \mathbf{x} and time t . The initial and boundary conditions are given

$$\lambda_1(\mathbf{x}, t = T) = \lambda_2(\mathbf{x}, t = T) = 0, \quad \text{in } \Omega \quad \lambda_1(\mathbf{x}, t) = \lambda_2(\mathbf{x}, t) = 0, \quad \text{on } \partial\Omega \times [0, T].$$

Then the gradient of the loss function (3.3) is

$$\begin{aligned} \nabla_{\theta_1, \theta_2} \mathcal{L} &= \int_0^T \int_{\Omega} -\lambda_2 \operatorname{div} \left(\frac{\partial \kappa_2(\mathbf{x}; \theta_1)}{\partial \theta_1} \nabla u_2(\mathbf{x}, t) \right) d\mathbf{x} dt \\ &+ \int_0^T \int_{\Omega} \lambda_1 \frac{\partial \sigma(\mathbf{x}; \theta_2)}{\partial \theta_2} (u_1(\mathbf{x}, t) - u_2(\mathbf{x}, t)) + \lambda_2 \frac{\partial \sigma(\mathbf{x}; \theta_2)}{\partial \theta_2} (u_2(\mathbf{x}, t) - u_1(\mathbf{x}, t)) d\mathbf{x} dt. \end{aligned} \quad (3.16)$$

The derivation procedure of the adjoint equation (3.15) is shown in **Appendix A**. By this means, we calculate the derivative $\nabla_{\theta_1, \theta_2} \mathcal{L}$ by solving the adjoint PDE and calculating the derivatives $\frac{\partial \kappa_2(\mathbf{x}; \theta_1)}{\partial \theta_1}$ and $\frac{\partial \sigma(\mathbf{x}; \theta_2)}{\partial \theta_2}$ through the automatic differentiation.

We calculate the numerical solution of adjoint equation (3.15) also by FEM. The discretization is

$$\begin{aligned} M \frac{\partial \lambda_1}{\partial t} - A_1(\kappa_1^*) \lambda_1 - \sigma(\mathbf{x}; \theta_2) M (\lambda_1 - \lambda_2) &= M(u - U), \\ M \frac{\partial \lambda_2}{\partial t} - A_2(\kappa_2(\mathbf{x}; \theta_1)) \lambda_2 - \sigma(\mathbf{x}; \theta_2) M (\lambda_2 - \lambda_1) &= 0, \end{aligned} \quad (3.17)$$

where A_1, A_2 are the stiffness matrices matrices, and M is the mass matrix, as shown in Section 3.2. The gradient (3.16) can be reformulated as

$$\begin{aligned} \nabla_{\theta_1, \theta_2} \mathcal{L} &= \int_T^0 \lambda_2^T \nabla_{\theta_1} A_2(\kappa_2) u_2 dt \\ &+ \int_T^0 \lambda_1^T \nabla_{\theta_2} \sigma(\theta_2) M (u_1 - u_2) dt \\ &+ \int_T^0 \lambda_2^T \nabla_{\theta_2} \sigma(\theta_2) M (u_2 - u_1) dt. \end{aligned} \quad (3.18)$$

Optimization for nonlinear equation with PINN solver. For the nonlinear multi-continuum model (3.2), PINN is used as our PDE solver as discussed in section 3.2.2, it avoids the iterations when using FEM and the Newton-Raphson method. The network parameters θ_1, θ_2 and θ_3 are optimized by direct BP in which the derivatives are calculated by automatic differentiation.

4. Experiments

In this section, we will present some numerical experiments and demonstrate the performance of the proposed learning-based multi-continuum model. Consider the flow equation on a unit square domain $\Omega = [0, 1] \times [0, 1] \subset \mathbb{R}^2$. In the following experiments, we apply zero Dirichlet boundary conditions and zero initial conditions. The reference solutions are obtained by averaging the fine-scale solution over each coarse block. The trusted data are sampled from the reference solutions. Further discussion on the trusted data can be found in **Appendix B**.

We calculate the numerical solution of PDE (3.2) by FEM. The loss function (3.3) is reformulated as

$$\mathcal{L} = \frac{\sum_{i,j=1}^{N_m} \sum_{n=1}^{N_t} (u(\mathbf{x}_i, t_n) - U(\mathbf{x}_i, t_n))^T M_{ij} (u(\mathbf{x}_j, t_n) - U(\mathbf{x}_j, t_n))}{\sum_{i,j=1}^{N_m} \sum_{n=1}^{N_t} U(\mathbf{x}_i, t_n)^T M_{ij} U(\mathbf{x}_j, t_n)} \times 100\%, \quad (4.1)$$

where $\{u(\mathbf{x}_i, t_n), U(\mathbf{x}_i, t_n)\}_{i=1, n=1}^{N_m, N_t}$ are numerical solutions of our proposed model and the trusted data respectively, and M_{ij} is corresponding element of the mass matrix.

Model architecture. The κ -net is employed to learn the permeability field of the second continuum. In the subsequent experiments, the κ -net is a multi-layer perceptron (MLP) with 5 hidden layers. The number of hidden neurons is set to 100 and the activation function is Tanh in each hidden layer. In order to ensure that the permeability matrix κ_2 is a positive definite matrix for all coordinates and times, the κ -net $\kappa_2(\mathbf{x}, t; \theta_1)$ is constrained to learn only the diagonal elements, with the additional requirement that they be greater than 0. Specifically, the learned permeability field $\kappa_2(\mathbf{x}, t; \theta_1) = \begin{pmatrix} \kappa_2^{11}(\mathbf{x}, t; \theta_1) & 0 \\ 0 & \kappa_2^{22}(\mathbf{x}, t; \theta_1) \end{pmatrix}$, and the absolute value function is taken as the activation function in the output layer to constrain $\kappa_2^{11}(\mathbf{x}, t; \theta_1) > 0, \kappa_2^{22}(\mathbf{x}, t; \theta_1) > 0$.

The σ -net learns transfer coefficients for our learning-based multi-continuum model. The σ -net used in our experiments is an MLP comprising 5 hidden layers, with *LeakyReLU* as the activation function and 100 hidden neurons per hidden layer. The *LeakyReLU* function is defined as

$$\text{LeakyReLU}(x) = \begin{cases} x, & x > 0, \\ cx, & x \leq 0. \end{cases}$$

We set $c = 0.2$ in all experiments.

In our experiment of nonlinear flow equations, the PINN solver is adopted and parameterized as an MLP with 7 hidden layers. The number of hidden neurons is 100, and the activation function is Tanh. Furthermore, the homogenized permeability κ_1^* represents the average value of each sub-domain in Ω . To calculate the homogenized permeability for each grid point, a convolution operation is employed to act as an interpolation function, with a convolution kernel size of 2×2 . The elements of this kernel are fixed as a constant value of $1/4$, without training.

Hyperparameters. The spatial partition Γ_h is the uniform mesh of the computational domain Ω , and the mesh size is set $h = 0.1$. The number of linear basis functions used in FEM is the same as the number of mesh points. We optimize the network parameters by Adam algorithm [25], and the learning rate is set to 1×10^{-4} . The total simulation time T and the time step size τ are separately presented in each of subsections 4.1-4.3.

4.1. Example 1: Linear flow equation

In the first example, the configuration of the permeability field and the source term $f(\mathbf{x})$ are shown in **Figure 2** (a-b). The value of permeability is 100 in the channel and 1 in the background. The homogenized equation is obtained by numerical homogenization, where the homogenized permeability $\kappa_1^* = \begin{pmatrix} \kappa_{11}^* & \kappa_{12}^* \\ \kappa_{21}^* & \kappa_{22}^* \end{pmatrix}$. The diagonal elements κ_{11}^*

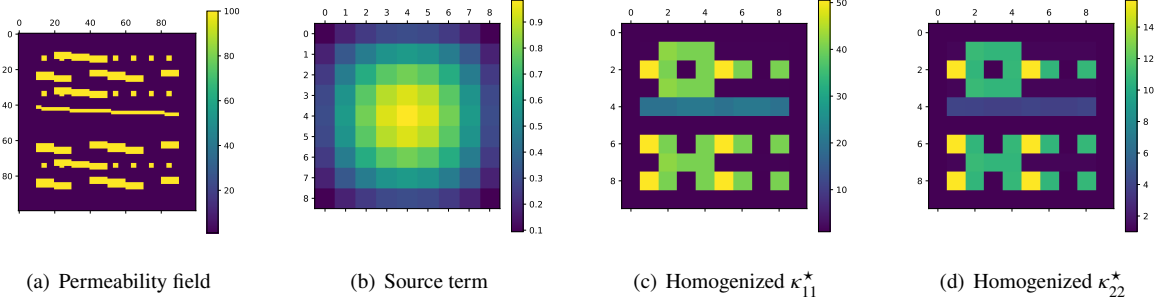


Figure 2: The configuration of the permeability field and the source term of the linear flow equation. (a) The permeability field on the fine grid. (b) The source term. (c) The value κ_{11}^* of the homogenized permeability. (d) The value κ_{22}^* of the homogenized permeability.

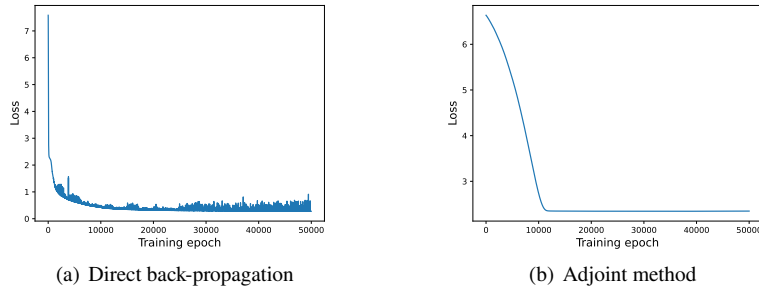


Figure 3: The training trajectories of the loss function. The gradients of network parameters are calculated by (a) direct BP and (b) the adjoint method.

and κ_{22}^* are shown in **Figure 2** (c-d), which are globally consistent with the configuration of the original permeability field. The total simulation time $T = 1$ and the time step size $\tau = 0.1$.

The gradients of the loss function (4.1) with respect to the network parameters are calculated using both direct BP and the adjoint method to optimize the proposed learning-based multi-continuum model (3.5). **Figure 3** shows the training trajectories of the loss function under two gradient calculation methods. It is evident that the loss function decreases rapidly and saturates after 12000 epochs for both methods. While direct BP can achieve a loss function of $O(10^{-1})$, the adjoint method can reach a loss function of $O(1)$.

Table 1 lists the relative L_2 error of the homogenized solutions and corrected solutions of our learning-based multi-continuum model with respect to the reference solutions. It can be seen that the numerical homogenization results in a significant relative L_2 error for each time step, which accumulates over time. The relative L_2 error increases from 5.7956% at time $t = 0.1$ to 7.7845% at time $t = 1$. However, our proposed learning-based multi-continuum model corrects the homogenized equation resulting in more accurate numerical solutions. The relative L_2 error of our multi-continuum model optimized by direct BP decreased from 0.1162% ($t = 0.1$) to 0.1084% ($t = 1$). The multi-continuum model optimized by the adjoint method for gradient calculation performs relatively poorly, with a relative L_2 error of approximately 2.33% for all time steps. **Figure 4** further displays the reference solutions, homogenized solutions, and the multi-continuum model's solutions at different time steps. Note that all of these solutions are FEM solutions. The figure reflects that our proposed learning-based multi-continuum model corrects the homogenized equation and generates the numerical solutions that closely match the reference solutions.

Figure 5 visualises the values of learned permeability $\kappa_2(\mathbf{x}; \theta_1)$ and the learned transfer coefficient $\sigma(\mathbf{x}; \theta_2)$. As discussed in **model architecture** of Section 4, the learned permeability $\kappa_2(\mathbf{x}, \theta_1) = \begin{pmatrix} \kappa_2^{11}(\mathbf{x}, \theta_1) & 0 \\ 0 & \kappa_2^{22}(\mathbf{x}, \theta_1) \end{pmatrix}$.

Table 1

The relative L_2 error (in percentage) of the homogenized solutions and solutions of the proposed multi-continuum model with respect to the reference solutions.

Method \ Time	0.1	0.2	0.3	0.4	0.5	0.6	0.7	0.8	0.9	1.0
Homogenization	5.7956	7.0050	7.5187	7.7016	7.7560	7.7774	7.7824	7.7838	7.7841	7.7845
Multi-continuum model (direct BP)	0.1162	0.1148	0.1106	0.1091	0.1086	0.1085	0.1084	0.1084	0.1084	0.1084
Multi-continuum model (adjoint method)	2.3355	2.3451	2.3379	2.3338	2.3321	2.3314	2.3311	2.3310	2.3310	2.3310

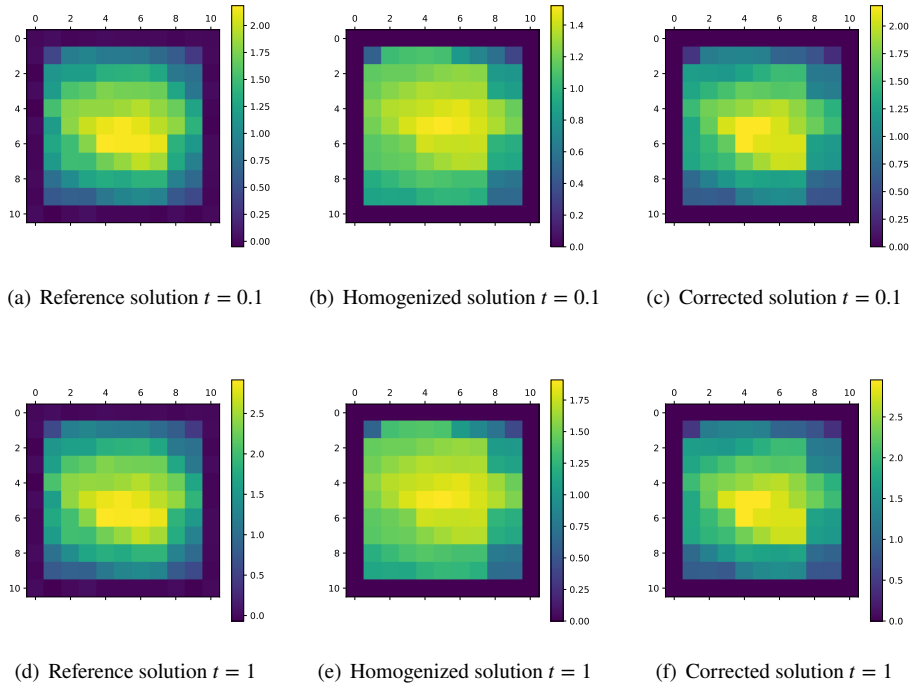


Figure 4: The FEM solutions of the linear flow equation, the homogenized equation and our proposed learning-based multi-continuum equation. (a)(d) The reference solutions at $t = 0.1$ and 1. (b)(e) The homogenized solutions at $t = 0.1$ and 1. (c)(f) The solutions of our proposed multi-continuum equation at $t = 0.1$ and 1.

Figure 5 (a-b) shows the diagonal elements $\kappa_2^{11}(\mathbf{x}, \theta_1)$ and $\kappa_2^{22}(\mathbf{x}, \theta_1)$. It can be seen that these two values have the same trend in the domain Ω , gradually increasing from the upper left corner to the lower right corner, but with relatively small increases. As illustrated in Figure 2 (c-d), the homogenized permeability field retains some average information of the original permeability field (Figure 2 (a)), while the learned permeability field κ_2 (Figure 5 (a-b)) represents some missing or overestimate information from κ_1^* . These two flow equations are composited into a new multi-continuum model in which the background and the fracture are written separately with some interaction. This multi-continuum model more accurately characterizes the complex dynamics within fractured media. **Figure 5** (c) shows the learned transfer coefficient $\sigma(\theta_2)$. The absolute values of σ are relatively small at the center of Ω , which reflects that the correction of the homogenized equation by the second continuum is relatively weaker in the center region of Ω . In other words, the numerical homogenization for this linear problem can portray the variation of the flow in the central region.

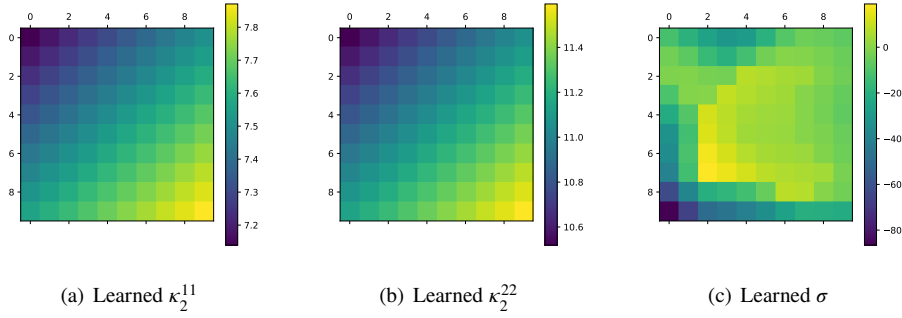


Figure 5: The learned permeability field κ_2 and transfer coefficient σ . (a-b) The diagonal elements κ_2^{11} and κ_2^{22} in domain Ω . (c) The learned transfer coefficient σ in domain Ω .

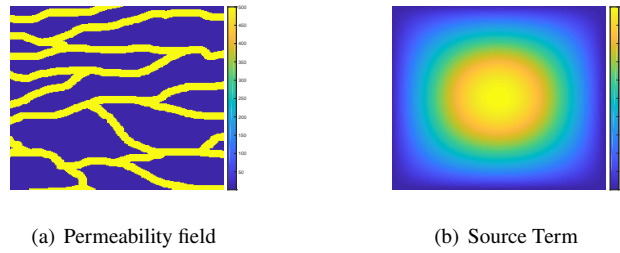


Figure 6: The configuration of the permeability field and the source term. (a) The permeability field. (b) The source term.

Table 2

The relative L_2 error (in percentage) of the homogenized solutions and solutions of the proposed multi-continuum model with respect to the reference solutions.

Method \ Time	0.0001	0.0002	0.0003	0.0004	0.0005	0.0006	0.0007	0.0008	0.0009	0.001
Homogenization	1.2710	2.2432	3.3052	4.4189	5.5602	6.7125	7.8634	9.0037	10.1263	11.2255
Multi-continuum model	0.5731	0.7715	0.9768	1.1847	1.3851	1.5715	1.7423	1.8996	2.0491	2.1995

4.2. Example 2: Linear flow equation with complex permeability field

The configuration of the permeability field and the source term $f(\mathbf{x})$ for this example are shown in **Figure 6**. This permeability field is closer to the real underground scene and is more complex. The value of permeability is 500 in the channel and 1 in the background. The homogenized equation is obtained by numerical homogenization. The total simulation time $T = 0.001$ and the time step size $\tau = 0.0001$.

Table 2 lists the relative L_2 error of the homogenized solutions and the corrected solutions of our multi-continuum model with respect to the reference solutions. The relative L_2 error of the homogenized solutions of this problem gradually increases over time, from 1.2710% at $t = 0.0001$ to 11.2255% at $t = 0.001$. Our learning-based multi-continuum model can correct the homogenized equation resulting in a small relative L_2 error. At time $t = 0.001$, the relative L_2 error of our multi-continuum model's solution is 2.1995%, which is one-fifth of the relative L_2 error for numerical homogenization. Meanwhile, the results reflect that our learning-based multi-continuum model reduces the accumulation of errors in the numerical solutions over time. **Figure 7** illustrates the numerical solutions of the original multiscale flow equation, the homogenized equation, and our proposed multi-continuum model at different time steps. The results demonstrate that our learning-based multi-continuum model effectively corrects the homogenized solutions and can capture the dynamics of the flow equation with this complex permeability field.

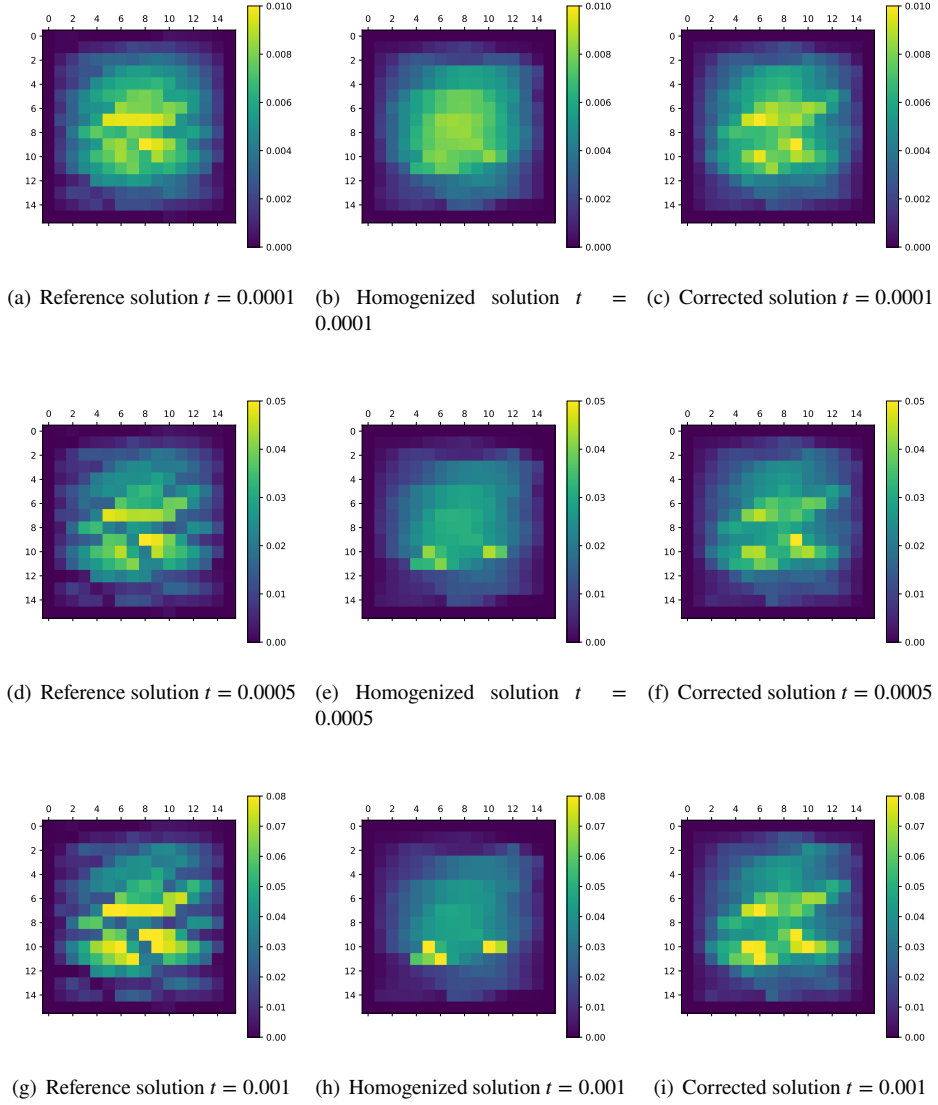


Figure 7: The FEM solutions of the flow equation with complex permeability field, the homogenized equation and our proposed learning-based multi-continuum equation at time $t = 0.0001, 0.0005, 0.001$. (a)(d)(g) The reference solutions. (b)(e)(h) The homogenized solutions. (c)(f)(i) The corrected solutions.

Figure 8 illustrates the values of the learned permeability $\kappa_2(\mathbf{x}; \theta_1)$ and the learned transfer coefficient $\sigma(\mathbf{x}; \theta_2)$. The diagonal elements $\kappa_2^{11}(\mathbf{x}; \theta_1)$ and $\kappa_2^{22}(\mathbf{x}; \theta_1)$ of the learned permeability are shown in **Figure 8** (a-b). It is apparent that these two values vary throughout the whole domain Ω , but the variation is relatively small. Similar to the first example, the learned permeability can be served to find the missing/over-estimated information for the numerical homogenization. **Figure 8** (c) displays the learned transfer coefficient $\sigma(\mathbf{x}; \theta_2)$ throughout the entire domain Ω . The result shows that the region of significant sigma fluctuations corresponds to the area of fluid flow alteration, while changes in the peripheral region are gradual, and the values are relatively small. These values of the learned transfer coefficient σ reflect the impact of adding the second continuum to the numerical homogenization.

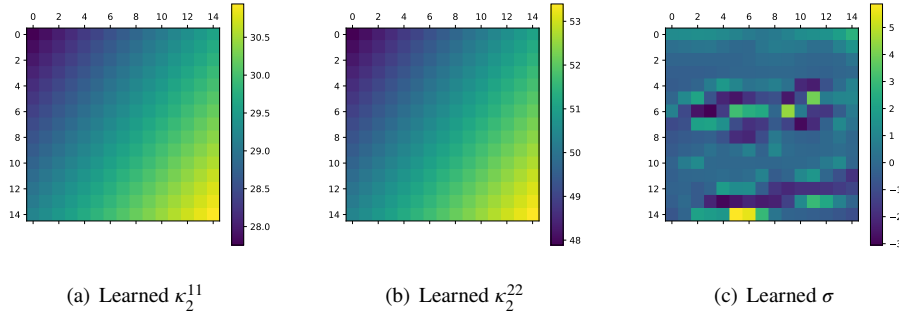


Figure 8: The learned permeability field κ_2 and transfer coefficient σ . (a-b) The diagonal elements κ_2^{11} and κ_2^{22} in domain Ω . (c) The learned σ .

Table 3

The relative L_2 error (in percentage) of the homogenized solutions and solutions of the proposed multi-continuum model with respect to the reference solutions.

Method \ Time	0.001	0.002	0.003	0.004	0.005	0.006	0.007	0.008	0.009	0.01
Homogenization	57.4263	50.9699	46.1707	42.4819	39.5630	37.1998	35.2499	33.6150	32.2250	31.0292
Multi-continuum model	0.6265	0.2800	0.0993	0.0343	0.0169	0.0132	0.0105	0.0061	0.0037	0.0124

4.3. Example 3: Nonlinear flow equation with discontinuous source term

In the example of the nonlinear equation, the permeability field $\kappa(\mathbf{x}, u(\mathbf{x}, t)) = a(\mathbf{x})e^{\beta u(\mathbf{x}, t)}$, and β is set to 0.01, which has relatively weak nonlinearity. The source term $f(\mathbf{x}, t)$ is a point source term. The configuration of the permeability field and the source term can be found in **Figure 9**. The conductivity is 10^4 in the channel and 1 in the background. Similar to before, we show the diagonal elements κ_{11}^* and κ_{22}^* of the homogenized permeability in **Figure 9** (c-d). Note we only show the permeability at time $t = 0$, because the equation is relatively weakly nonlinear and the permeability changes with time are very small. The total simulation time $T = 0.01$ and the time step size $\tau = 0.001$.

The PINN is used as the PDE solver for the nonlinear flow equation, and network parameters are optimized through direct BP. Networks are trained for 300000 epochs and the loss function (3.13) can reach $O(10^{-3})$. **Figure 10** shows examples of the reference solutions, homogenized solutions, and the corrected solutions of our multi-continuum model. It can be seen that numerical homogenization can capture the overall dynamics of flow, with relatively large errors. In contrast, our learning-based multi-continuum model corrects the homogenized equation and results in more accurate solutions. **Table 3** lists the relative L_2 error of our corrected solutions and homogenized solutions with respect to reference solutions at each time step. The corrected solutions obtained by our multi-continuum model are very close to the true solution, with the relative L_2 errors all within 1%. While the relative L_2 error of the numerical homogenization reaches 57.4263% at time 0.001.

Figure 11 further illustrates the values of the learned permeability $\kappa_2(\mathbf{x}, t; \theta_1)$ and the learned transfer coefficient $\sigma(\mathbf{x}, t; \theta_2)$ for the nonlinear flow equation, which are all dependent on the time t . The diagonal elements κ_2^{11} and κ_2^{22} in the whole domain Ω at time $t = 0.001$ and 0.01 are shown in **Figure 11** (a-d). It can be observed that κ_2^{11} and κ_2^{22} vary very little over time and the values of κ_2^{11} and κ_2^{22} are also closely grouped across the domain Ω . These results further indicate that the newly introduced continuum in the multi-continuum model can complement the information obtained from the numerical homogenization. The learned coefficient σ at time 0.001 and 0.01 is illustrated in **Figure 11** (e-f). It can be seen that σ has essentially the same trend across the region at different time steps. The absolute values of σ are larger all in places where the flow fluctuates more.

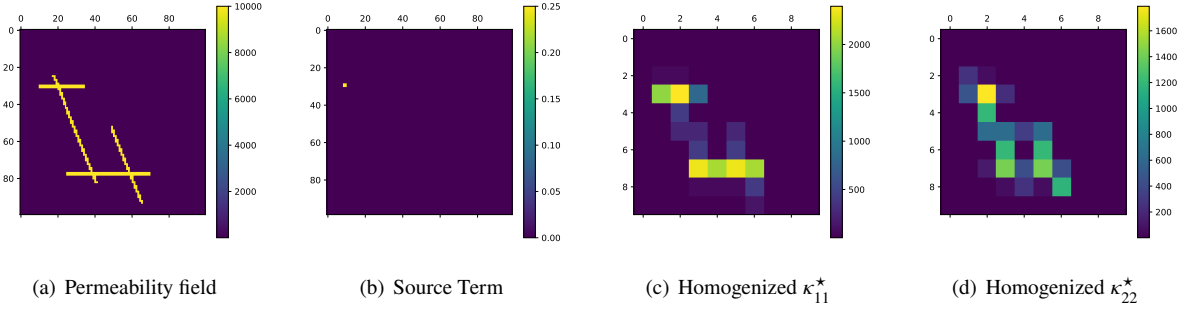


Figure 9: The configuration of the permeability field and the point source term. (a) The permeability field. (b) The point source term. (c) The homogenized permeability κ_{11}^* . (d) The homogenized permeability κ_{22}^* .

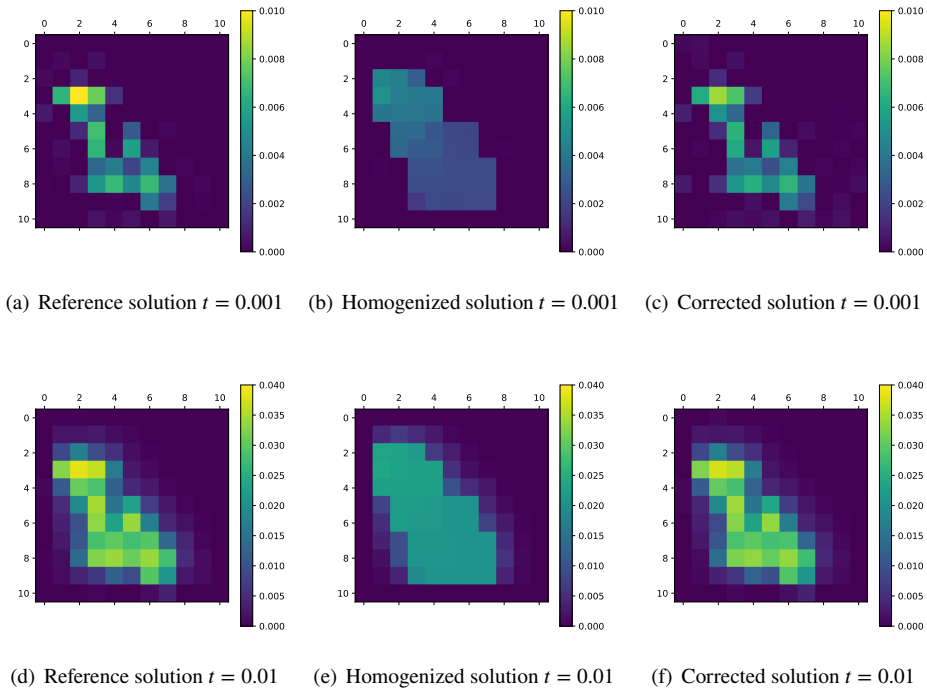


Figure 10: The FEM solutions of the nonlinear flow equation, the homogenized equation and our proposed learning-based multi-continuum equation. (a)(d) The reference solutions at $t = 0.001, 0.01$; (b)(e) The homogenized solutions at $t = 0.001, 0.01$; (c)(f) The corrected solutions at $t = 0.001, 0.01$;

5. Conclusion

In this paper, we propose a novel learning-based multi-continuum model for complex multiscale problems to correct solutions obtained through numerical homogenization and improve their accuracy. Without loss of generalization, we consider a two-continuum case. We reformulate the homogenized equation as a multi-continuum model, with the flow equation for the first continuum retaining the information of the original homogenized equation, along with an additional interaction term. The second continuum's flow equation necessitates the use of a neural network to determine its effective permeability. The interaction term between the two continua is aligned with that of the Dual-porosity model but with a learnable coefficient determined by another neural network. Using trusted data, i.e., accurate solutions at

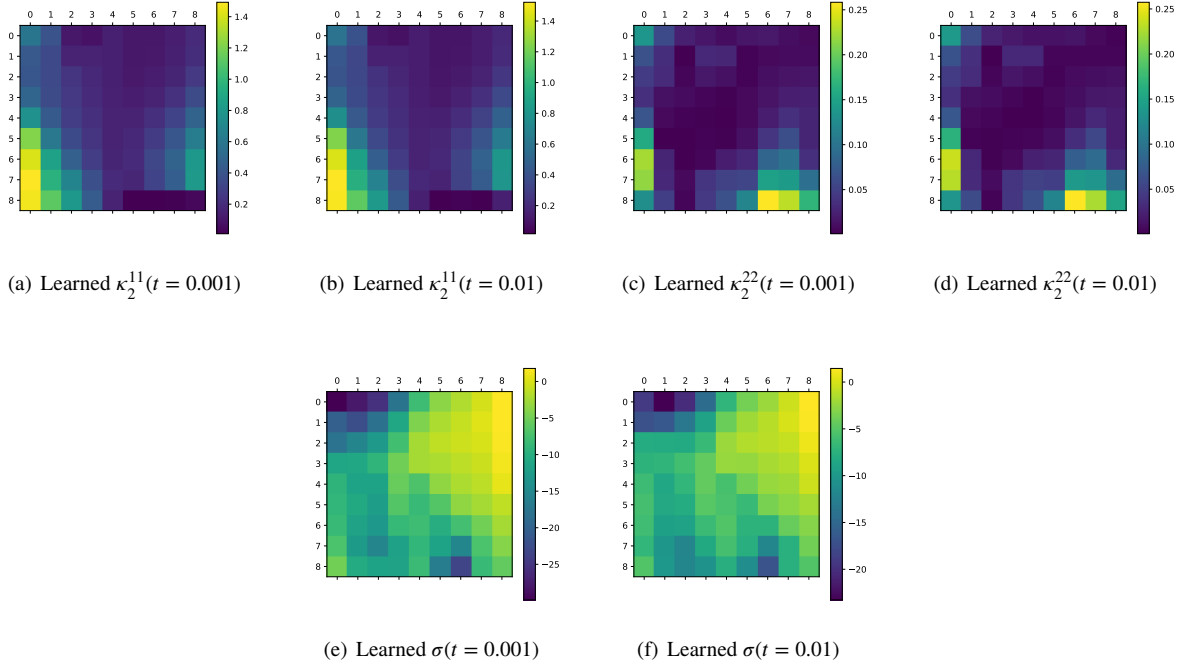


Figure 11: The learned permeability field κ_2 and transfer coefficient σ . (a-d) The diagonal elements κ_2^{11} and κ_2^{22} at time $t = 0.001$ and 0.01 in domain Ω . (e-f) The learned transfer coefficient σ at time $t = 0.001$ and 0.01 .

some points, we optimize these two neural networks by minimizing the mismatch between the numerical solutions of the multi-continuum model and the trusted data. We further discuss both direct back-propagation and the adjoint method for the PDE-constraint optimization problem. Our proposed learning-based multi-continuum model can resolve multiple interacted media within each coarse grid block and describe the mass transfer among them by introducing a new continuum to complement the missing/over-estimated information of the numerical homogenization. Numerical experiments demonstrate that our proposed learning-based multi-continuum model can correct the solutions obtained through numerical homogenization and improve their accuracy.

Acknowledgments

This work was supported by National Natural Science Foundation of China (grant no. 12301559) and Hong Kong RGC Early Career Scheme (grant no. 9048274).

Appendix

A. Derivation of adjoint equation. The loss function is given by

$$\mathcal{L} = \frac{1}{2} \int_0^T \int_{\Omega} \|u_1(\mathbf{x}, t) - U(\mathbf{x}, t)\|^2 dx dt. \quad (.1)$$

The first step is to introduce the Lagrangian corresponding to the optimization problem:

$$\begin{aligned}
 \mathcal{L} \equiv & \int_0^T \int_{\Omega} \frac{1}{2} \|u_1(\mathbf{x}, t) - U(\mathbf{x}, t)\|^2 + \lambda_1(\mathbf{x}, t) \left[\frac{\partial u_1(\mathbf{x}, t)}{\partial t} - \operatorname{div}(\kappa_1^*(\mathbf{x}) \nabla u_1(\mathbf{x}, t)) + \sigma(\mathbf{x}; \theta_2)(u_1(\mathbf{x}, t) - u_2(\mathbf{x}, t)) - f(\mathbf{x}, t) \right] \\
 & + \lambda_2(\mathbf{x}, t) \left[\frac{\partial u_2(\mathbf{x}, t)}{\partial t} - \operatorname{div}(\kappa_2(\mathbf{x}; \theta_1) \nabla u_2(\mathbf{x}, t)) + \sigma(\mathbf{x}; \theta_2)(u_2(\mathbf{x}, t) - u_1(\mathbf{x}, t)) \right] dx dt + \int_{\Omega} \mu_1 u_1(\mathbf{x}, 0) + \mu_2 u_2(\mathbf{x}, 0) dx \\
 & + \int_0^T \int_{\partial\Omega} \mu_3 u_1(\mathbf{x}, t) + \mu_4 u_2(\mathbf{x}, t) dx dt.
 \end{aligned} \tag{.2}$$

The Lagrangian multipliers λ_1 and λ_2 is a function of time t and coordinate x , and $\mu_1, \mu_2, \mu_3, \mu_4$ are other multipliers that are associated with the initial and boundary conditions.

$$\begin{aligned}
 \frac{\partial \mathcal{L}}{\partial \theta_1} = & \int_0^T \int_{\Omega} (u_1(\mathbf{x}, t) - U(\mathbf{x}, t)) \frac{\partial u_1}{\partial \theta_1} dx dt \\
 & + \int_0^T \int_{\Omega} \lambda_1 \left[\frac{\partial^2 u_1(\mathbf{x}, t)}{\partial \theta_1 \partial t} - \frac{\partial}{\partial \theta_1} \operatorname{div}(\kappa_1^*(\mathbf{x}) \nabla u_1(\mathbf{x}, t)) + \sigma(\mathbf{x}; \theta_2) \left(\frac{u_1(\mathbf{x}, t)}{\partial \theta_1} - \frac{u_2(\mathbf{x}, t)}{\partial \theta_1} \right) \right] dx dt \\
 & + \int_0^T \int_{\Omega} \lambda_2 \left[\frac{\partial^2 u_2(\mathbf{x}, t)}{\partial \theta_1 \partial t} - \frac{\partial}{\partial \theta_1} \operatorname{div}(\kappa_2(\mathbf{x}; \theta_1) \nabla u_2(\mathbf{x}, t)) + \sigma(\mathbf{x}; \theta_2) \left(\frac{u_2(\mathbf{x}, t)}{\partial \theta_1} - \frac{u_1(\mathbf{x}, t)}{\partial \theta_1} \right) \right] dx dt \\
 & + \int_{\Omega} \mu_1 \frac{\partial u_1(\mathbf{x}, 0)}{\partial \theta_1} + \mu_2 \frac{\partial u_2(\mathbf{x}, 0)}{\partial \theta_1} dx + \int_0^T \int_{\partial\Omega} \mu_3 \frac{\partial u_1(\mathbf{x}, t)}{\partial \theta_1} + \mu_4 \frac{\partial u_2(\mathbf{x}, t)}{\partial \theta_1} dx dt.
 \end{aligned} \tag{.3}$$

The next step is to integrate by parts to eliminate the terms $\frac{\partial^2 u_1(\mathbf{x}, t)}{\partial \theta_1 \partial t}$ and $\frac{\partial^2 u_2(\mathbf{x}, t)}{\partial \theta_1 \partial t}$:

$$\begin{aligned}
 & \int_0^T \int_{\Omega} \lambda_1 \left[\frac{\partial^2 u_1(\mathbf{x}, t)}{\partial \theta_1 \partial t} - \frac{\partial}{\partial \theta_1} \operatorname{div}(\kappa_1^*(\mathbf{x}) \nabla u_1(\mathbf{x}, t)) \right] dx dt \\
 = & \int_{\Omega} \left(\lambda_1 \frac{\partial u_1(\mathbf{x}, t)}{\partial \theta_1} \Big|_0^T - \int_0^T \frac{\partial u_1(\mathbf{x}, t)}{\partial \theta_1} \frac{\partial \lambda_1}{\partial t} dt \right) dx - \int_0^T \int_{\Omega} \frac{\partial u_1(\mathbf{x}, t)}{\partial \theta_1} \operatorname{div}(\kappa_1^*(\mathbf{x}) \nabla \lambda_1) dx dt \\
 = & \int_0^T \int_{\Omega} -\frac{\partial u_1(\mathbf{x}, t)}{\partial \theta_1} \frac{\partial \lambda_1}{\partial t} - \frac{\partial u_1(\mathbf{x}, t)}{\partial \theta_1} \operatorname{div}(\kappa_1^*(\mathbf{x}) \nabla \lambda_1) dx dt - \int_{\Omega} \lambda_1(\mathbf{x}, 0) \frac{\partial u_1(\mathbf{x}, 0)}{\partial \theta_1} dx,
 \end{aligned} \tag{.4}$$

where the transformation in the second and third line use the Divergence Theorem, and we let the boundary condition $\lambda_1(\mathbf{x}, t)|_{\partial\Omega} = 0$ and final condition $\lambda_1(\mathbf{x}, T) = 0$. The same result can be obtained for u_2 , i.e.,

$$\begin{aligned}
 & \int_0^T \int_{\Omega} \lambda_2 \left[\frac{\partial^2 u_2(\mathbf{x}, t)}{\partial \theta_1 \partial t} - \frac{\partial}{\partial \theta_1} \operatorname{div}(\kappa_2(\mathbf{x}; \theta_1) \nabla u_2(\mathbf{x}, t)) \right] dx dt \\
 = & \int_0^T \int_{\Omega} -\frac{\partial u_2(\mathbf{x}, t)}{\partial \theta_1} \frac{\partial \lambda_2}{\partial t} - \frac{\partial u_2(\mathbf{x}, t)}{\partial \theta_1} \operatorname{div}(\kappa_2(\mathbf{x}; \theta_1) \nabla \lambda_2) dx dt \\
 & - \int_0^T \int_{\Omega} \lambda_2 \operatorname{div} \left(\frac{\kappa_2(\mathbf{x}; \theta_1)}{\partial \theta_1} \nabla u_2(\mathbf{x}, t) \right) dx dt - \int_{\Omega} \lambda_2(\mathbf{x}, 0) \frac{\partial u_2(\mathbf{x}, 0)}{\partial \theta_1} dx.
 \end{aligned} \tag{.5}$$

Substituting these results into equation (.3),

$$\begin{aligned}
 \frac{\partial \mathcal{L}}{\partial \theta_1} &= \int_0^T \int_{\Omega} (u_1(\mathbf{x}, t) - U(\mathbf{x}, t)) \frac{\partial u_1}{\partial \theta_1} dx dt \\
 &+ \int_0^T \int_{\Omega} -\frac{\partial u_1(\mathbf{x}, t)}{\partial \theta_1} \frac{\partial \lambda_1}{\partial t} - \frac{\partial u_1(\mathbf{x}, t)}{\partial \theta_1} \operatorname{div}(\kappa_1^*(\mathbf{x}) \nabla \lambda_1) + \lambda_1 \sigma(\mathbf{x}; \theta_2) \left(\frac{u_1(\mathbf{x}, t)}{\partial \theta_1} - \frac{u_2(\mathbf{x}, t)}{\partial \theta_1} \right) dx dt \\
 &+ \int_0^T \int_{\Omega} -\frac{\partial u_2(\mathbf{x}, t)}{\partial \theta_1} \frac{\partial \lambda_2}{\partial t} - \frac{\partial u_2(\mathbf{x}, t)}{\partial \theta_1} \operatorname{div}(\kappa_2(\mathbf{x}, \theta_1) \nabla \lambda_2) - \lambda_2 \operatorname{div} \left(\frac{\kappa_2(\mathbf{x}, \theta_1)}{\partial \theta_1} \nabla u_2(\mathbf{x}, t) \right) dx dt \\
 &+ \int_0^T \int_{\Omega} \lambda_2 \sigma(\mathbf{x}; \theta_2) \left(\frac{u_2(\mathbf{x}, t)}{\partial \theta_1} - \frac{u_1(\mathbf{x}, t)}{\partial \theta_1} \right) dx dt + \int_{\Omega} \mu_1 \frac{\partial u_1(\mathbf{x}, 0)}{\partial \theta_1} + \mu_2 \frac{\partial u_2(\mathbf{x}, 0)}{\partial \theta_1} dx \\
 &- \int_{\Omega} \lambda_1(\mathbf{x}, 0) \frac{\partial u_1(\mathbf{x}, 0)}{\partial \theta_1} dx - \int_{\Omega} \lambda_2(\mathbf{x}, 0) \frac{\partial u_2(\mathbf{x}, 0)}{\partial \theta_1} dx + \int_0^T \int_{\partial \Omega} \mu_3 \frac{\partial u_1(\mathbf{x}, t)}{\partial \theta_1} + \mu_4 \frac{\partial u_2(\mathbf{x}, t)}{\partial \theta_1} dx dt.
 \end{aligned} \tag{.6}$$

We set $\mu_1 = \lambda_1(\mathbf{x}, 0)$ and $\mu_2 = \lambda_2(\mathbf{x}, 0)$, $\mu_3 = \mu_4 = 0$ to cancel the last four terms. The calculation of gradient $\frac{\partial u_1(\mathbf{x}, t)}{\partial \theta_1}$ and $\frac{\partial u_2(\mathbf{x}, t)}{\partial \theta_1}$ can be avoided by setting

$$\begin{aligned}
 \frac{\partial \lambda_1}{\partial t} + \operatorname{div}(\kappa_1^*(\mathbf{x}) \nabla \lambda_1) - \sigma(\mathbf{x}; \theta_2)(\lambda_1 - \lambda_2) &= u_1(\mathbf{x}, t) - U(\mathbf{x}, t), \\
 \frac{\partial \lambda_2}{\partial t} + \operatorname{div}(\kappa_2(\mathbf{x}, \theta_1) \nabla \lambda_2) - \sigma(\mathbf{x}; \theta_2)(\lambda_2 - \lambda_1) &= 0.
 \end{aligned} \tag{.7}$$

This is the obtained adjoint equation with the initial condition $\lambda_1(\mathbf{x}, t = T) = \lambda_2(\mathbf{x}, t = T) = 0$ and boundary condition $\lambda_1(\mathbf{x}, t)|_{\partial \Omega} = \lambda_2(\mathbf{x}, t)|_{\partial \Omega} = 0$. Finally the gradient can be obtained by

$$\frac{\partial \mathcal{L}}{\partial \theta_1} = \int_0^T \int_{\Omega} -\lambda_2 \operatorname{div} \left(\frac{\kappa_2(\mathbf{x}, \theta_1)}{\partial \theta_1} \nabla u_2(\mathbf{x}, t) \right) dx dt. \tag{.8}$$

The similar derivation can be applied for θ_2 and the obtained adjoint equation is the same as equation (.7). The desired gradient are given by

$$\frac{\partial \mathcal{L}}{\partial \theta_2} = \int_0^T \int_{\Omega} \lambda_1 \frac{\partial \sigma(\mathbf{x}; \theta_2)}{\partial \theta_2} (u_1(\mathbf{x}, t) - u_2(\mathbf{x}, t)) + \lambda_2 \frac{\partial \sigma(\mathbf{x}; \theta_2)}{\partial \theta_2} (u_2(\mathbf{x}, t) - u_1(\mathbf{x}, t)) dx dt. \tag{.9}$$

In this way, the network parameters θ_1 and θ_2 can be optimized by classical optimization method, such as gradient descent method. In the integral formulations, (.8) and (.9), the derivatives $\frac{\kappa_2(\mathbf{x}, \theta_1)}{\partial \theta_1}$ and $\frac{\partial \sigma(\mathbf{x}; \theta_2)}{\partial \theta_2}$ can be calculated by the automatic differentiation of Pytorch/Tensorflow.

Further, we calculate the numerical solutions of adjoint equation by FEM. The corresponding discretization of adjoint equation is given by

$$\begin{aligned}
 M \frac{\partial \lambda_1}{\partial t} - A_1(\kappa_1^*) \lambda_1 - \sigma(\theta_2) M (\lambda_1 - \lambda_2) &= M(u - U), \\
 M \frac{\partial \lambda_2}{\partial t} - A_2(\kappa_2(\theta_1)) \lambda_2 - \sigma(\theta_2) M (\lambda_2 - \lambda_1) &= 0,
 \end{aligned} \tag{.10}$$

where A_1, A_2 are the stiffness matrices, and M is the mass matrix. The gradient of the loss function is reformulated as

$$\begin{aligned}
 \nabla_{\theta_1, \theta_2} \mathcal{L} &= \int_T^0 \lambda_2^T \nabla_{\theta_1} A_2(\kappa_2) u_2 dt \\
 &+ \int_T^0 \lambda_1^T \nabla_{\theta_2} \sigma(\theta_2) M (u_1 - u_2) dt \\
 &+ \int_T^0 \lambda_2^T \nabla_{\theta_2} \sigma(\theta_2) M (u_2 - u_1) dt.
 \end{aligned} \tag{.11}$$

Table 4

The relative L_2 error (in percentage) of the homogenized solutions and solutions of the proposed multi-continuum model with respect to the reference solutions when the trusted data are sampled in time.

Method \ Time	0.1	0.2	0.3	0.4	0.5	0.6	0.7	0.8	0.9	1.0
Homogenization	5.7956	7.0050	7.5187	7.7016	7.7560	7.7774	7.7824	7.7838	7.7841	7.7845
Our model	train				test					
	0.1290	0.1285	0.1119	0.1138	0.1145	0.1148	0.1149	0.1149	0.1149	0.1149
Our model	train				test					
	0.1251	0.1218	0.1130	0.1084	0.1137	0.1142	0.1143	0.1143	0.1143	0.1143

Table 5

The relative L_2 error (in percentage) of the homogenized solutions and solutions of the proposed multi-continuum model with respect to the reference solutions when the trusted data are sampled in space. Sampling ratios are listed in parentheses.

Method \ Time	0.1	0.2	0.3	0.4	0.5	0.6	0.7	0.8	0.9	1.0
Homogenization	5.7956	7.0050	7.5187	7.7016	7.7560	7.7774	7.7824	7.7838	7.7841	7.7845
Our model (60%)	0.2415	0.2331	0.2303	0.2293	0.2290	0.2289	0.2288	0.2288	0.2288	0.2288
Our model (70%)	0.1634	0.1630	0.1655	0.1669	0.1674	0.1676	0.1677	0.1677	0.1677	0.1677
Our model (80%)	0.1533	0.1523	0.1554	0.1573	0.1581	0.1583	0.1584	0.1584	0.1584	0.1584
Our model (100%)	0.1162	0.1148	0.1106	0.1091	0.1086	0.1085	0.1084	0.1084	0.1084	0.1084

B. The details on the trusted data and the reference solutions. The reference solutions are obtained by averaging the fine-scale solutions over each coarse block. In the above experiments in Section 4, the trusted data used to train neural networks are the whole reference solutions. This is because our proposed method is designed not only to correct the homogenized solution but also to obtain a novel multi-continuum model, which more accurately characterizes the intricate dynamics within fractured media. Here we conduct further experiments to evaluate the performance of our proposed method when the trusted data is sampled from the reference solutions.

The initial stage of the experiments involves sampling the trusted data in time from the reference solution. The results are presented in Table 4. It can be observed that the relative L_2 error exhibits a slight reduction with more time steps sampled (from $t = 0.4$ to $t = 0.6$). This outcome reflects that as the number of sampled time steps increases, the model is able to characterize the dynamics with greater accuracy and obtain more precise solutions. Furthermore, the observed reduction in error is relatively modest, indicating that our method is capable of learning a robust model from a limited amount of time-step data.

Furthermore, the trusted data were randomly sampled from the reference solutions at 60%, 70%, and 80% of the total space, respectively, and all time steps were used. The results are listed in Table 5. It can be seen that there is a significant increase in the relative L_2 error of the solution obtained by our model with fewer trusted data sampled in space. This indicates that our approach is reliant on the presence of a greater density of data in space. Furthermore, it can be postulated that the sampling strategy employed may also influence the results. In the current experiment, the trusted data were sampled from a uniform distribution. Should the sampling points be concentrated in the more variable regions of the dynamical system, it may be possible to achieve a performance improvement with less data. The impact of alternative sampling techniques, such as importance sampling, can be evaluated in future work.

References

- [1] Aarnes, J.E., Efendiev, Y., 2008. Mixed multiscale finite element methods for stochastic porous media flows. *SIAM Journal on Scientific Computing* 30, 2319–2339.
- [2] Aarnes, J.E., Efendiev, Y., Jiang, L., 2008. Mixed multiscale finite element methods using limited global information. *Multiscale Modeling & Simulation* 7, 655–676.
- [3] Abdassah, D., Ershaghi, I., 1986. Triple-porosity systems for representing naturally fractured reservoirs. *SPE Formation Evaluation* 1, 113–127.

- [4] Abdulle, A., Weinan, E., Engquist, B., Vanden-Eijnden, E., 2012. The heterogeneous multiscale method. *Acta Numerica* 21, 1–87.
- [5] Allaire, G., 1992. Homogenization and two-scale convergence. *SIAM Journal on Mathematical Analysis* 23, 1482–1518. URL: <https://doi.org/10.1137/0523084>, doi:10.1137/0523084.
- [6] Allaire, G., Brizzi, R., 2005. A multiscale finite element method for numerical homogenization. *Multiscale Modeling & Simulation* 4, 790–812.
- [7] Babuška, I., 1976. Homogenization and its application. mathematical and computational problems, in: HUBBARD, B. (Ed.), *Numerical Solution of Partial Differential Equations* CIII. Academic Press, pp. 89–116. URL: <https://www.sciencedirect.com/science/article/pii/B9780123585035500099>, doi:<https://doi.org/10.1016/B978-0-12-358503-5.50009-9>.
- [8] Bai, M., Elsworth, D., Roegiers, J.C., 1993. Multiporosity/multipermeability approach to the simulation of naturally fractured reservoirs. *Water Resources Research* 29, 1621–1633.
- [9] Barenblatt, G.I., Zheltov, I.P., Kochina, I., 1960. Basic concepts in the theory of seepage of homogeneous liquids in fissured rocks [strata]. *Journal of applied mathematics and mechanics* 24, 1286–1303.
- [10] Benner, P., Gugercin, S., Willcox, K., 2015. A survey of projection-based model reduction methods for parametric dynamical systems. *SIAM review* 57, 483–531.
- [11] Bradley, A.M., 2013. PDE-constrained optimization and the adjoint method. Technical Report. Technical Report. Stanford University. <https://cs.stanford.edu/~ambrad...>
- [12] Chaturantabut, S., Sorensen, D.C., 2010. Nonlinear model reduction via discrete empirical interpolation. *SIAM Journal on Scientific Computing* 32, 2737–2764.
- [13] Cheung, S.W., Chung, E.T., Efendiev, Y., Gildin, E., Wang, Y., Zhang, J., 2020. Deep global model reduction learning in porous media flow simulation. *Computational Geosciences* 24, 261–274.
- [14] Chinesta, F., Ladeveze, P., Cueto, E., 2011. A short review on model order reduction based on proper generalized decomposition. *Archives of Computational Methods in Engineering* 18, 395–404.
- [15] Efendiev, Y., Galvis, J., Hou, T.Y., 2013. Generalized multiscale finite element methods (gmsfem). *Journal of computational physics* 251, 116–135.
- [16] Efendiev, Y., Galvis, J., Wu, X.H., 2011. Multiscale finite element methods for high-contrast problems using local spectral basis functions. *Journal of Computational Physics* 230, 937–955.
- [17] Efendiev, Y., Hou, T.Y., 2009. *Multiscale finite element methods: theory and applications*. volume 4. Springer Science & Business Media.
- [18] Engquist, B., Sogkanidis, P.E., 2008. Asymptotic and numerical homogenization. *Acta Numerica* 17, 147–190.
- [19] Fan, Y., Lin, L., Ying, L., Zepeda-Núñez, L., 2019. A multiscale neural network based on hierarchical matrices. *Multiscale Modeling & Simulation* 17, 1189–1213.
- [20] Henning, P., Målqvist, A., 2014. Localized orthogonal decomposition techniques for boundary value problems. *SIAM Journal on Scientific Computing* 36, A1609–A1634.
- [21] Henning, P., Peterseim, D., 2013. Oversampling for the multiscale finite element method. *Multiscale Modeling & Simulation* 11, 1149–1175.
- [22] Hinze, M., Volkwein, S., 2005. Proper orthogonal decomposition surrogate models for nonlinear dynamical systems: Error estimates and suboptimal control, in: *Dimension Reduction of Large-Scale Systems: Proceedings of a Workshop held in Oberwolfach, Germany, October 19–25, 2003*, Springer. pp. 261–306.
- [23] Hughes, T.J., Feijóo, G.R., Mazzei, L., Quincy, J.B., 1998. The variational multiscale method: a paradigm for computational mechanics. *Computer methods in applied mechanics and engineering* 166, 3–24.
- [24] Jikov, V.V., Kozlov, S.M., Oleinik, O.A., 2012. *Homogenization of differential operators and integral functionals*. Springer Science & Business Media.
- [25] Kingma, D.P., Ba, J., 2014. Adam: A method for stochastic optimization. arXiv preprint arXiv:1412.6980.
- [26] Leung, W.T., Lin, G., Zhang, Z., 2022. Nh-pinn: Neural homogenization-based physics-informed neural network for multiscale problems. *Journal of Computational Physics* 470, 111539. URL: <https://www.sciencedirect.com/science/article/pii/S0021999122006015>, doi:<https://doi.org/10.1016/j.jcp.2022.111539>.
- [27] Li, Z., Kovachki, N., Azizzadenesheli, K., Liu, B., Bhattacharya, K., Stuart, A., Anandkumar, A., 2020. Fourier neural operator for parametric partial differential equations. arXiv preprint arXiv:2010.08895.
- [28] Lu, L., Jin, P., Pang, G., Zhang, Z., Karniadakis, G.E., 2021. Learning nonlinear operators via deepnet based on the universal approximation theorem of operators. *Nature machine intelligence* 3, 218–229.
- [29] Målqvist, A., Peterseim, D., 2014. Localization of elliptic multiscale problems. *Mathematics of Computation* 83, 2583–2603.
- [30] Miller, S.T., Roberts, N.V., Bond, S.D., Cyr, E.C., 2022. Neural-network based collision operators for the boltzmann equation. *Journal of Computational Physics* 470, 111541. URL: <https://www.sciencedirect.com/science/article/pii/S0021999122006039>, doi:<https://doi.org/10.1016/j.jcp.2022.111541>.
- [31] Nguetseng, G., 1989. A general convergence result for a functional related to the theory of homogenization. *SIAM Journal on Mathematical Analysis* 20, 608–623. URL: <https://doi.org/10.1137/0520043>, doi:10.1137/0520043.
- [32] Raissi, M., Perdikaris, P., Karniadakis, G.E., 2019. Physics-informed neural networks: A deep learning framework for solving forward and inverse problems involving nonlinear partial differential equations. *Journal of Computational physics* 378, 686–707.
- [33] Sirignano, J., MacArt, J., Spiliopoulos, K., 2023. Pde-constrained models with neural network terms: Optimization and global convergence. *Journal of Computational Physics* 481, 112016. URL: <https://www.sciencedirect.com/science/article/pii/S0021999123001110>, doi:<https://doi.org/10.1016/j.jcp.2023.112016>.
- [34] Sirignano, J., MacArt, J.F., Freund, J.B., 2020. Dpm: A deep learning pde augmentation method with application to large-eddy simulation. *Journal of Computational Physics* 423, 109811. URL: <https://www.sciencedirect.com/science/article/pii/S0021999120305854>, doi:<https://doi.org/10.1016/j.jcp.2020.109811>.

- [35] Sirignano, J., Spiliopoulos, K., 2018. Dgm: A deep learning algorithm for solving partial differential equations. *Journal of computational physics* 375, 1339–1364.
- [36] Wang, Y., Cheung, S.W., Chung, E.T., Efendiev, Y., Wang, M., 2020. Deep multiscale model learning. *Journal of Computational Physics* 406, 109071.
- [37] Wu, Y.S., Qin, G., Ewing, R.E., Efendiev, Y., Kang, Z., Ren, Y., 2006. A multiple-continuum approach for modeling multiphase flow in naturally fractured vuggy petroleum reservoirs, in: *SPE International Oil and Gas Conference and Exhibition in China, SPE*. pp. SPE-104173.
- [38] Xiao, T., Frank, M., 2023. Relaxnet: A structure-preserving neural network to approximate the boltzmann collision operator. *Journal of Computational Physics* 490, 112317. URL: <https://www.sciencedirect.com/science/article/pii/S0021999123004126>, doi:<https://doi.org/10.1016/j.jcp.2023.112317>.
- [39] Yu, B., et al., 2018. The deep ritz method: a deep learning-based numerical algorithm for solving variational problems. *Communications in Mathematics and Statistics* 6, 1–12.
- [40] Zhu, Y., Zabaras, N., Koutsourelakis, P.S., Perdikaris, P., 2019. Physics-constrained deep learning for high-dimensional surrogate modeling and uncertainty quantification without labeled data. *Journal of Computational Physics* 394, 56–81.